*metals*

MDPI

*Article*

# Static Recrystallization Behavior and Texture Evolution during Annealing in a Cold Rolling Beta Titanium Alloy Sheet

**Shuzhi Zhang [1,*], Qibin Wang [2], Xing Cheng [1], Jianchao Han [3], Wanggang Zhang [1], Changjiang Zhang [1] and Jie Wu [4,*]**

[1] College of Materials Science and Engineering, Taiyuan University of Technology, Taiyuan 030024, China; chengxing@tyut.edu.cn (X.C.); zhangshuzhi@tyut.edu.cn (W.Z.); zhangcj@tyut.edu.cn (C.Z.)
[2] College of Materials Science and Engineering, Harbin Institute of Technology, Harbin 150001, China; wangqibin@hit.edu.cn
[3] College of Mechanical and Vehicle Engineering, Taiyuan University of Technology, Taiyuan 030024, China; hanjc@tyut.edu.cn
[4] College of Architecture, Taiyuan University of Technology, Taiyuan 030024, China
* Correspondence: shuzhizhang@outlook.com (S.Z.); wujie@tyut.edu.cn (J.W.)

**Abstract:** In this study, the cold rolling microstructure and static recrystallization mechanism of the high strength titanium alloy Ti-3.5Al-5Mo-6V-3Cr-2Sn-0.5Fe were systematically investigated. Results show that the cold rolling microstructure is mainly composed of the elongated deformed β grains containing micro-shear bands. After annealing at 815 °C for 2 min, the fine SRXed grains are observed, mainly concentrated in the micro-shear band, the grain boundary and the interior of the deformed grain. The sub-grain structure obtained by static recovery inside the deformed grain produces continuous SRX during the annealing treatment. Meanwhile, geometric and discontinued SRXed grains are also observed in the large deformed β grain and at the trigeminal grain boundaries, respectively. Many ultra-fine grains appear inside the micro-shear band, exhibiting a phenomenon of the micro-shear band assisting SRX. With the increase in the annealing holding time, the elongated β grains are significantly refined and the degree of recrystallization is continuously improved. In addition, the recrystallization behavior also results in a significant change in the fiber texture. With the extension of the annealing holding time, the rolling texture type evolves gradually, with the {111}<112> γ-fiber texture to weak α-fiber, γ-fiber, and Goss-fiber.

**Keywords:** titanium alloy; cold rolling; annealing treatment; microstructure; recrystallization; texture

check for updates

**Citation:** Zhang, S.; Wang, Q.; Cheng, X.; Han, J.; Zhang, W.; Zhang, C.; Wu, J. Static Recrystallization Behavior and Texture Evolution during Annealing in a Cold Rolling Beta Titanium Alloy Sheet. *Metals* **2022**, *12*, 899. https://doi.org/10.3390/met12060899

Academic Editor: Håkan Hallberg

Received: 16 April 2022
Accepted: 23 May 2022
Published: 25 May 2022

**Publisher's Note:** MDPI stays neutral with regard to jurisdictional claims in published maps and institutional affiliations.

**Copyright:** © 2022 by the authors. Licensee MDPI, Basel, Switzerland. This article is an open access article distributed under the terms and conditions of the Creative Commons Attribution (CC BY) license (https://creativecommons.org/licenses/by/4.0/).

## 1. Introduction

With the rapid development of the modern aerospace industry, the demands for high strength and high plasticity structural materials are increasing in various fields [1–3]. High strength β titanium alloys with excellent combinations of strength, corrosion resistance and fatigue resistance are competitive candidates to be applied in the aerospace, automotive and biomedical industries [4–6]. However, the balance between strength and ductility limits the further application of the alloy [7,8].

Recrystallization, which has a critical influence on the microstructure and mechanical properties, is the main refinement mechanism of cold deformation β alloy. Previous studies through the refinement of β grains obtain outstanding strength and ductility [9,10]. The high strength β titanium alloy has the advantage of rollability, so the combination of cold rolling and recrystallization heat treatment can effectively refine β grain and improve the mechanical properties [11,12]. Du et al. [13] have reported that the Ti-3.5Al-5Mo-6V-3Cr-2Sn-0.5Fe alloy was investigated by cold rolling and annealing, finding that the β grain size was reduced and the mechanical properties were improved. Recrystallization heat treatment plays a key role in the optimization of microstructure and properties, whereas there is a lack of detailed analysis of the static recrystallization of β titanium alloy. Hence,

it is necessary to study the static recrystallization behavior of β titanium alloy after cold rolling and annealing.

It is currently widely accepted that the SRX (static recrystallization) mechanism can be divided into three categories, according to nucleation and growth characteristics: continuous static recrystallization (CSRX); discontinuous static recrystallization (DSRX) and geometric static recrystallization (GSRX). At the early stages of heat treatment, fine dislocation-free sub-grains are formed in deformation grain by static recovery (SRV) [14,15]. Then these sub-grain structures with low angle grain boundaries (LAGBs) will gradually transform into high angle grain boundaries (HAGBs) to form new grains [16]. This process without a nucleation stage is characterized by the continuous rotation of sub-grains accompanied by little accompanying boundary migration (mainly sub-grain boundary migration), which can be labeled as CSRX or extended recovery [17,18]. Additionally, GSRX was initially considered as one type of CSRX by Humpreys and Hatherly [19], whereas the characteristics of GSRX do differ from that of CSRX in many ways [20]. SRX can also take place uniformly, with the nucleation of new strain-free grains by the migration of HAGBs with a clear nucleation and growth stage, which can be classified as DSRX [15,16].

In this study, the effect of annealing heat treatment on the microstructure of beta type Ti alloy plate Ti-3.5Al-5Mo-6V-3Cr-2Sn-0.5Fe was investigated. A detailed analysis of the static recrystallization behavior during annealing occurring in cold rolling beta Ti alloy is conducted. Additionally, the texture evolution of the cold rolling microstructure during annealing heat treatment is also discussed.

## 2. Experimental Procedure

This high-strength β Titanium alloy is obtained by the vacuum arc remelting method (VAR), with a chemical composition of Ti-3.5Al-5Mo-6V-3Cr-2Sn-0.5Fe (in wt.%). Table 1 depicts the nominal and actual chemical composition. The α/β transition temperature of current composites is about 810 ± 5 °C, determined by the metallographic method.

**Table 1.** The chemical composition of Titanium ingots (wt.%).

| Elements | Al | Mo | V | Cr | Sn | Fe |
|---|---|---|---|---|---|---|
| Nominal content | 3.5 | 5 | 6 | 3 | 2 | 0.5 |
| Actual content | 3.61 | 5.26 | 5.71 | 2.97 | 1.91 | 0.494 |

To ensure the microstructure homogeneity and eliminate casting defects, the ingot was hot forged at 890 °C with a strain rate of 0.01 $s^{-1}$ on a conventional hydraulic press with a maximum force of 4 MN. Subsequently, rectangular solid specimens with dimension of 40 mm × 40 mm × 4 mm were wire-cut for cold-rolling from the as-forged billet. Before rolling, the solution heat-treatment (820 °C/30 min/water colling) process was used to obtain a single β phase alloy. The rolling process was carried out at room temperature with a strain rate of 0.05 $s^{-1}$. The specimens were cold rolled with a reduction of 10% per pass and with a total strain of 90%. Afterward, the specimens obtained from the cold-rolled alloy were annealed at 815 °C for different holding times (2, 5, 15, 30 min) followed by furnace cooling. For the sake of convenience, the specimens were designated as HT-1, HT-2, HT-3 and HT-4 with the increased heat treatment holding time, respectively. The detailed cold-rolling and the heat treatment process are presented in Figure 1. The cooling rate of this annealing treatment is about 10 °C/s, and the rate of temperature increase is about 15 °C/s. The annealing treatment is carried out in the atmosphere of Argon.

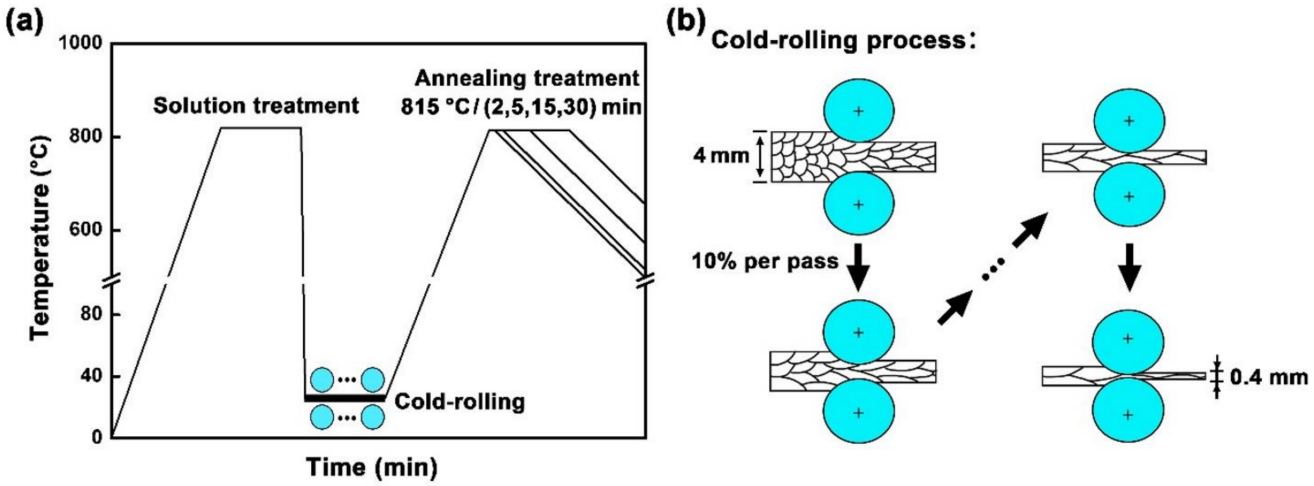


**Figure 1.** The working process and schematic diagram of cold-rolling: (**a**) the working process; (**b**) cold-rolling process.

The distribution and constitution of the phases were determined using optical microscopy (OM, Leica DM2700M, Weztlar, Germany) and electron backscatter diffraction (EBSD). The EBSD measurement was conducted on Quanta 200FEG scanning electron microscopy (FEI, Hillsboro, OR, USA) with an EBSD unit and the collected data were processed with Channel 5 analysis software. The EBSD specimens were ground on SiC papers first, and then followed by electropolishing procedure with the solution of 60% methanol, 30% 1-butanol and 10% perchloric acid (vol.%) at −5 °C~−10 °C.

## 3. Results and Discussion

### *3.1. Heat Treatment Microstructure Characteristic*

Figure 2 shows the optical micrographs (OM) of the alloy during cold rolling. As shown in Figure 2a, the cold rolling microstructure is mainly composed of elongated deformed β grains parallel to the rolling direction (RD). Besides, there are obvious micro-shear bands in the rolled microstructure. Generally, large grains have weak strain coordination ability in the polycrystalline system, which is more likely to form shear bands than small grains in the deformation process [21]. The microstructure of the cold rolling specimens after heat treatment are displayed in Figure 2b–e. The primary heat treatment, an annealing heat treatment, is performed at 815 °C for different holding times, followed by furnace cooling, whereby many fine SRXed grains are observed in the microstructure. It can be investigated that the specimen HT-1 (Figure 2b) exhibits the elongated deformed β grains and the fine SRXed grains. These fine SRXed grains are mainly concentrated in the micro-shear band, the grain boundary and the interior of the deformed grain (marked by black arrows and white fonts). As for the details of the local microstructure shown in the upper right corner, the fine SRXed grains are clearly found inside the micro-shear band and at the grain boundaries, respectively. It may be attributed to that, that the micro-shear band, large deformation grains and grain boundaries have high storage energy after cold rolling, where the SRX process occurs preferentially during the heat treatment [22]. With the extension of holding time, as shown in Figure 2c,d, the degree of SRX increases significantly, while the elongated β grains (un-SRXed grains) decrease continuously. When the holding time reaches 30 min (Figure 2e), the microstructure was transformed into fine equiaxed grains under sufficient time conditions, indicating complete recrystallization.

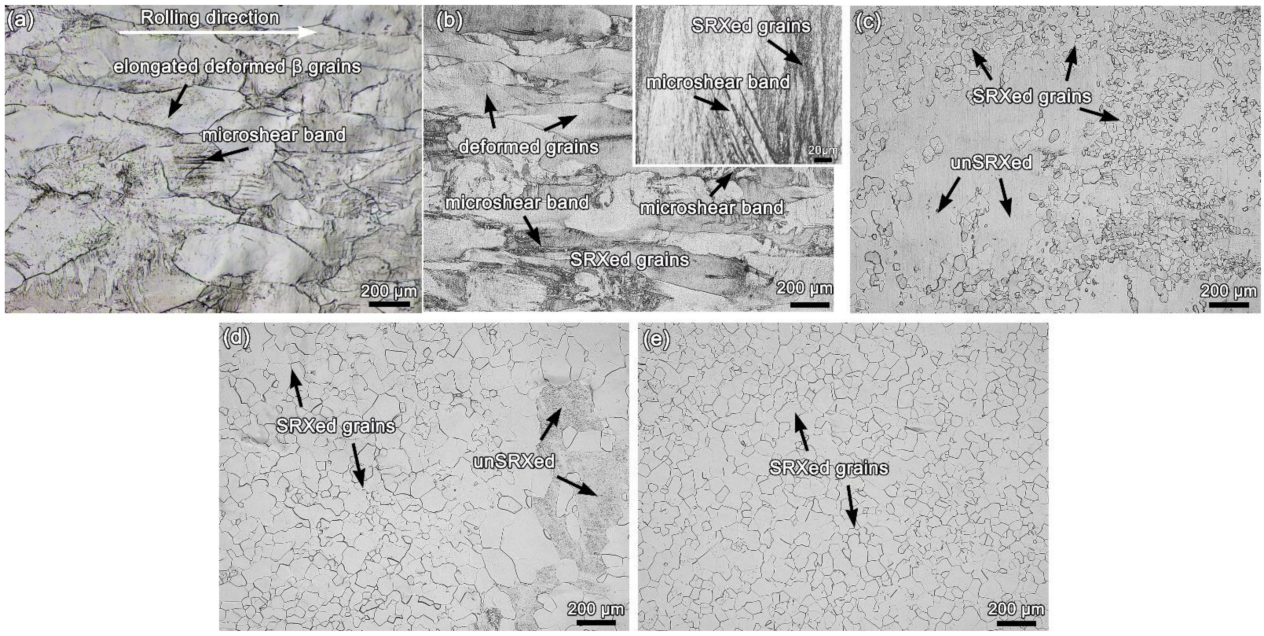


**Figure 2.** The OM micrographs of the alloy after different heat-treatments: (**a**) rolled microstructure; (**b**) HT-1; (**c**) HT-2; (**d**) HT-3; (**e**) HT-4.

### *3.2. SRX Behavior of the Deformed Grains*

In order to further discuss the microstructure evolution and the SRX process of the alloy, the specimen HT-1 is selected and characterized by the EBSD method in detail. Figure 3 shows the EBSD maps of the specimen HT-1, which focuses on the deformed β grain. Figure 3b, the inverse pole figure (IPF map) overlapped with grain boundaries, shows the characteristics of grain orientation and grain boundaries. By combined analysis with the band contrast map (BC map, Figure 3a) and the corresponding IPF map, plenty of sub-grain boundaries and SRXed grains are obtained after heat treatment. The sub-grain structures are obtained through the SRV process in the deformed β grain, where the CSRX may continue to occur during annealing. The significant chromatic aberration regions, which may imply the occurrence of CSRX, are investigated in the deformed β grain [23], such as the R1 and R2 regions marked in Figure 3b. Generally, the CSRX usually occurs in the inner of the deformed grains with the misorientation ranging from 10–15° [24–26]. Therefore, the CSRX can be evaluated by the point-to-origin (cumulative) misorientation and the point-to-point (local) misorientation along with the grain interior. According to this, the R1 and R2 regions with obvious misorientation are selected in Figure 3b to further discuss the CSRX mechanism. As shown in Figure 3d, the IPF map of the R1 region and the corresponding crystallographic three-dimensional orientation are depicted. The color of the R1 region mainly transitions from light blue- to dark blue, along the black arrow AB direction. Figure 3e displays the corresponding PF and IPF, highlighted with the same colors as Figure 3d. It can be determined that the light blue-colored region clusters at [021]//RD, while the relatively dark blue-colored region clusters around [−1–11]//RD. That is to say, the orientation gradually changes from [−1–11]//RD to [021]//RD during the continuous rotation of the sub-grain. According to the line profile of the arrow AB, the point-to-origin line reveals a cumulative misorientation that exceeds 10° (Figure 3f), while the line profile of the point-to-point maintains a small variation, indicating that the continuous rotation of the sub-grain causes the occurrence of CSRX. Meanwhile, as shown in Figure 3g–i, the misorientation angle along arrow CD also reveals that the occurrence of CSRX processes in the R2 region.

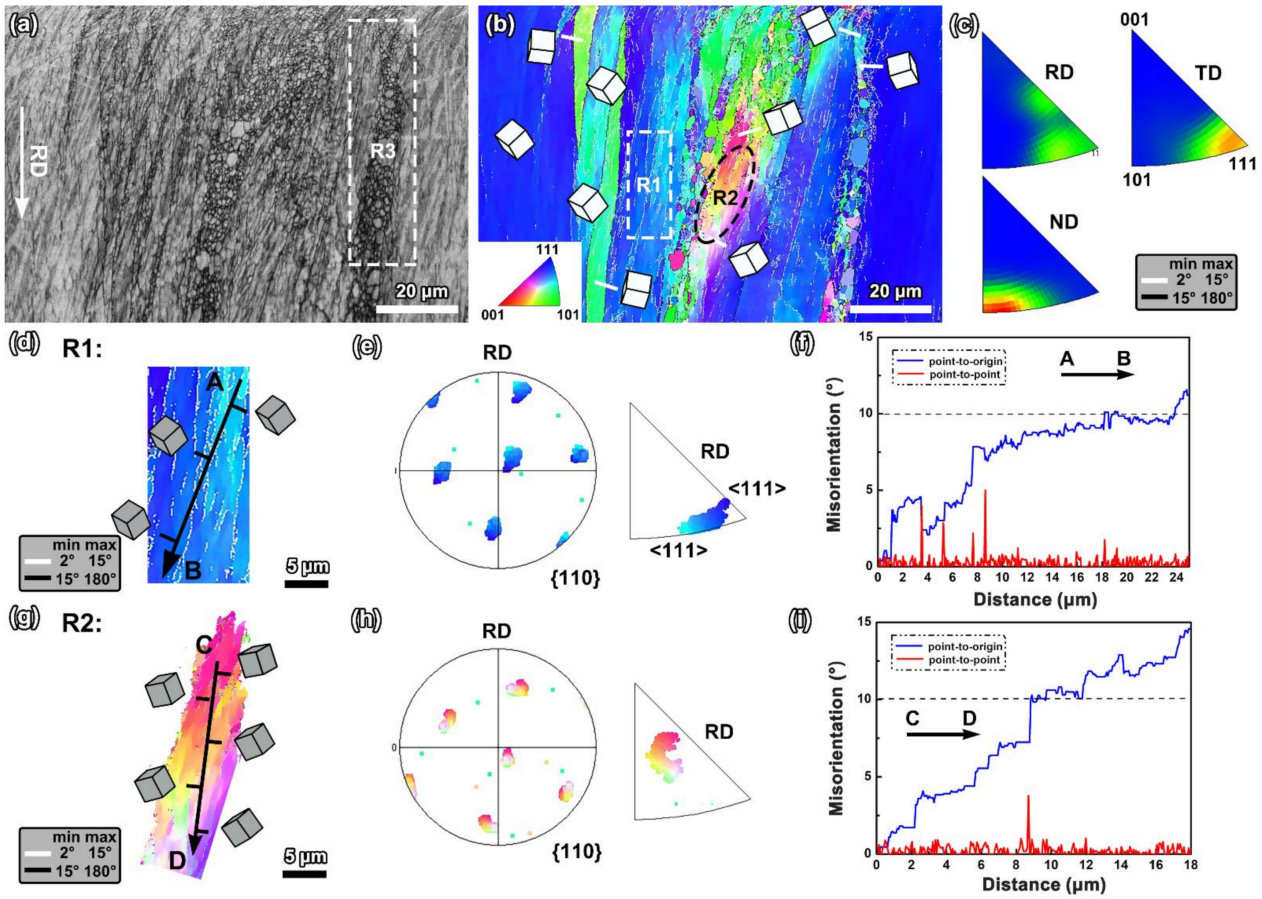


**Figure 3.** EBSD analysis of the specimen HT-1: (**a**) band contrast map (BC); (**b**) inverse pole figure (IPF); (**c**) pole figure (PF); (**d**,**g**) IPF map of R1 and R2 regions; (**e**,**h**) the corresponding (110) PF; (**f**,**i**) the misorientation angle along the black arrow AB and CD. Here, TD is the Transverse direction of sheet, ND is the Normal direction of the sheet, RD is the Rolling direction of the sheet, R3 is shown in Figure 3a.

Figure 4 presents the SRX behavior of the large deformation region, marked by a white dotted bordered rectangle in Figure 3a. As shown in Figure 4a, three elongated deformed β grains are defined as $\beta_1$, $\beta_2$ and $\beta_3$, respectively. Comparing with the $\beta_1$ grain and $\beta_3$ grain, the fine SRXed grains can be clearly observed in the $\beta_2$ grain with a larger strain. Figure 4c displays the characteristics of the grain boundaries which is exhibited by the high angle grain boundaries (HAGBs, >15°) marked with black lines and the low angle grain boundaries (LAGBs, 2–15°) marked with white lines. The HAGBs are normally the features of the SRXed grain boundaries, while the LAGBs are mainly concentrated in the sub-boundaries [27]. These sub-boundaries are formed by the dislocation rearrangement during SRV [28]. The corresponding kernel average misorientation (KAM) map is presented in Figure 4d, which depicts the local distortion distribution in grain. The region covered in green means the higher density of the geometrically necessary dislocation (GNDs), while the regular blue colored region indicates the lower GNDs density. The sub-boundaries with high GNDs density related to the SRV behavior are mainly concentrated in the deformed grains, whereas the low GNDs density or strain-free regions appear in the sub-grains and SRXed grains (depicted in Figure 5b,c). Figure 4e shows the near-equiaxed sub-grain structure rather than the fibrous sub-grain structure inside the $\beta_2$ grain, which is different from the elongated sub-grain of the CSRX process in Figure 3d,g. Combined with the analysis of Figure 4e–g, the misorientation angle of adjacent sub-grain boundaries measured from the point-to-point line profile exhibits low misorientations, implying the occurrence of the GSRX [29]. The GSRXed grains are obtained through (i) the migration

of HAGBs to form serrations, as marked by R3 in Figure 4b, resulting in the existence of the equiaxed sub-grain instead of the fibrous sub-grain, (ii) thinning of the grain thickness, which requires the formation of a larger deformed microstructure and the reduction of the grain thickness to approaching 1–2 sub-grain size distance, such as the $\beta_2$ grain [30–32]. Therefore, the existing differences between CSRX and GSRX, and the occurrence of GSRX require a greater degree of deformation to reach the critical strain.

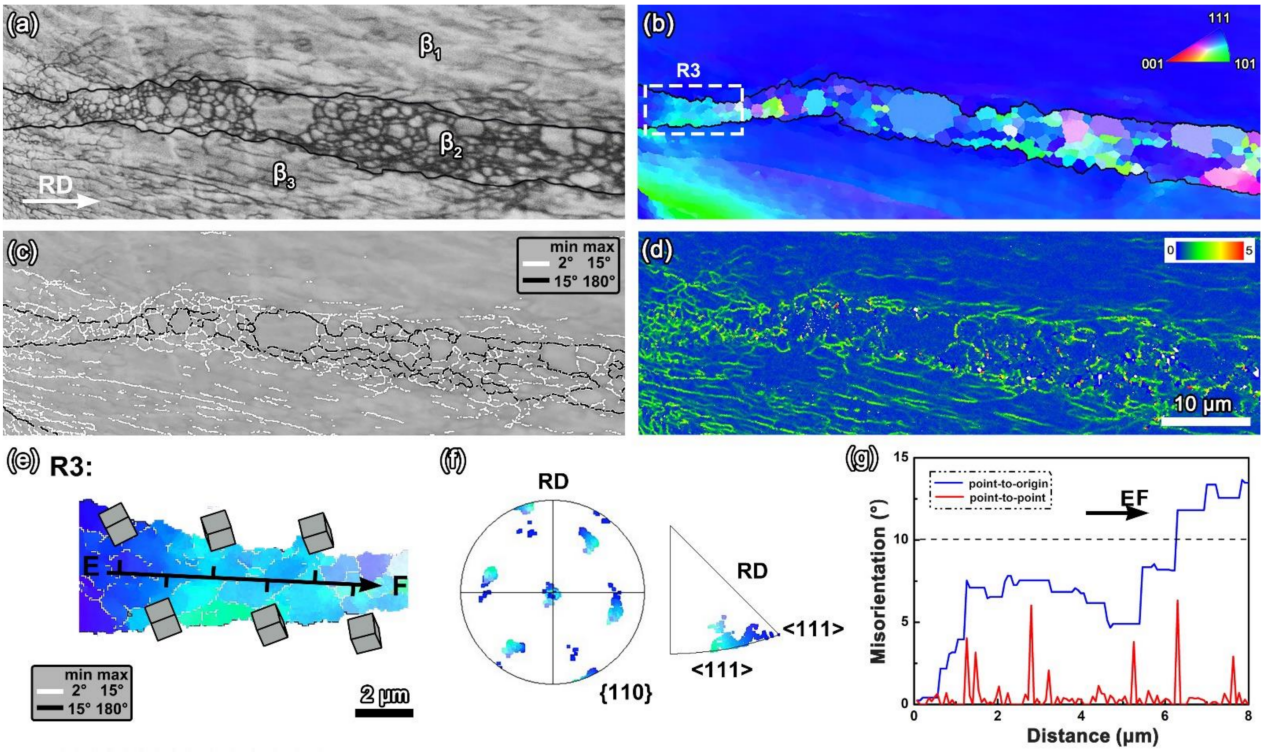


**Figure 4.** Analysis of geometric static recrystallization mechanism in the larger deformed β grain of specimen HT-1: (**a**) BC map; (**b**) IPF map; (**c**) grain boundaries misorientation; (**d**) KAM map; (**e**–**g**) the misorientation angle along black arrow EF and (110) pole figure.

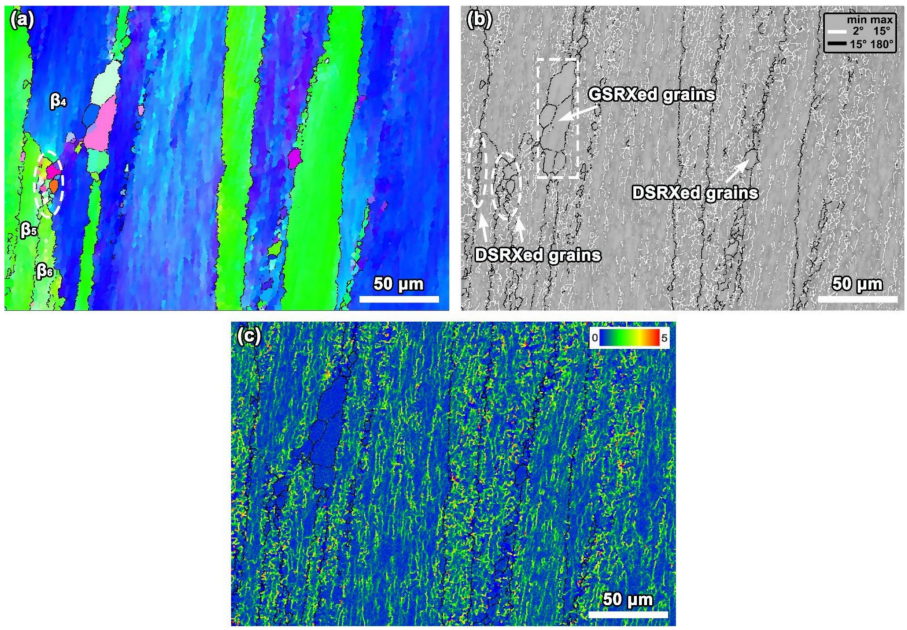


**Figure 5.** Analysis of discontinuous static recrystallization mechanism of specimen HT-1: (**a**) IPF map; (**b**) grain boundaries misorientation; (**c**) KAM map.

Figure 5 displays the recrystallization region situated at the deformed β grain boundaries. As shown in Figure 5a, the serrated grain boundary of the deformed β grains bulged toward the adjacent grains by migration of HAGBs, and a few of the fine SRXed grains exist at the triple junctions of the un-SRXed grains. This is a typical feature of DSRX. The KAM map (Figure 5c) reveals that the bulging of the original HAGBs absorbs the surrounding dislocations, leaving a region with low dislocation density behind the migration boundary [33]. The bulged areas are isolated by the sub-boundaries to form new DSRX grain along the serrated grain boundary, and then usually become the potential nucleation sites of the DSRX.

### *3.3. Microshear Band Assisted SRX*

Figure 6 presents the EBSD analysis results of the micro-shear band. As shown in Figure 6a,c, the microstructure morphology in the micro-shear band, where many ultra-fine grains can be observed, is completely different from that of the surrounding regions. As illustrated by Figure 6b,d, the region with the obvious chromatic aberration in the micro-shear band indicates the existence of the grain misorientation, whereas the surrounding regions exhibit a consistent orientation. This may be due to the SRX process that led to the random distribution of grain orientation. Combined with Figure 6($d_1$–$d_3$), the misorientation of the adjacent grains is greater than 15° (HAGBs), which confirms that new grains are obtained in the micro-shear band by SRX behavior. Therefore, the ultra-fine grained microstructure is formed by recrystallization during the annealing treatment after severe rolling deformation, exhibiting a phenomenon of micro-shear band-assisted SRX. However, this phenomenon mainly exists in the micro-shear band and does not occur homogeneously within the deformed β grain.

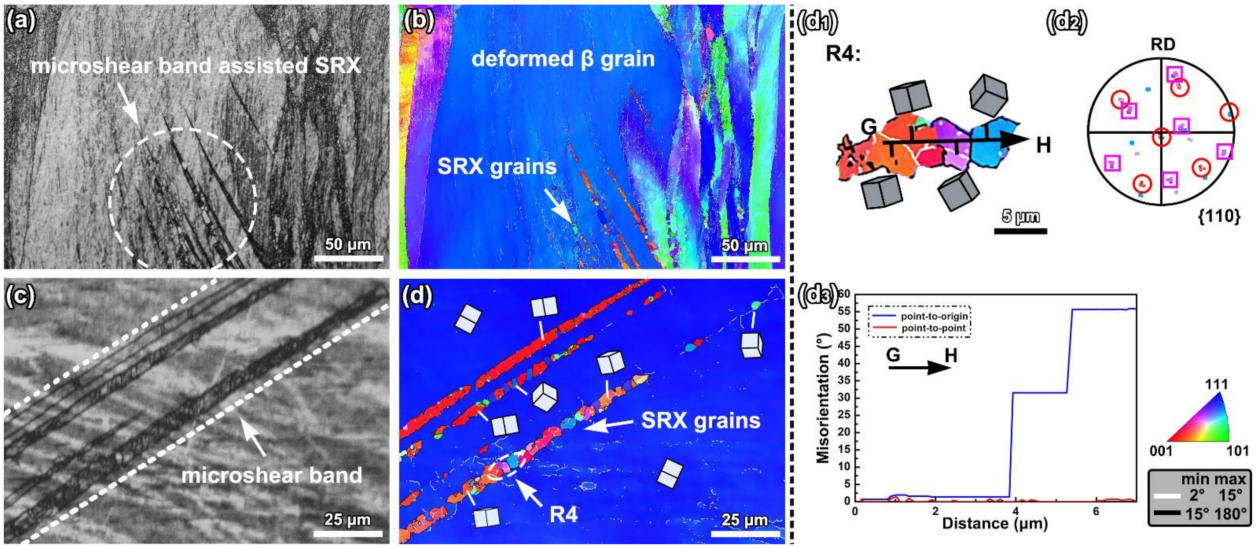


**Figure 6.** Analysis of static recrystallization mechanism in the micro-shear band of specimen HT-1: (**a**,**c**) band contrast (BC) maps; (**b**,**d**) IPF maps; (**$d_1$**) IPF map of the local region 1 within the micro-shear band; (**$d_2$**) corresponding PF map of the region 1; (**$d_3$**) the misorientation angle along with black arrow AB and corresponding pole figure.

Through the previous discussion, the cold rolling microstructure of the β Ti alloy exhibits various SRX behaviors that appear in different microstructure morphology during annealing, as shown in Figure 7. At the grain boundaries, especially at trigeminal grain boundaries, DSRX grains will be formed by grain boundary bulging during annealing. Inside the elongated deformed grain, the LAGBs are transformed into HAGBs by continuous rotation of the sub-grain to form CSRXed grain during the subsequent annealing treatment. In addition, GSRX may occur in the large deformation region, resulting in fine equiaxed recrystallized grains. Many ultra-fine grains appear inside the micro-shear band, which

is inhomogeneous within the deformed grain, exhibiting a phenomenon of micro-shear band-assisted SRX.

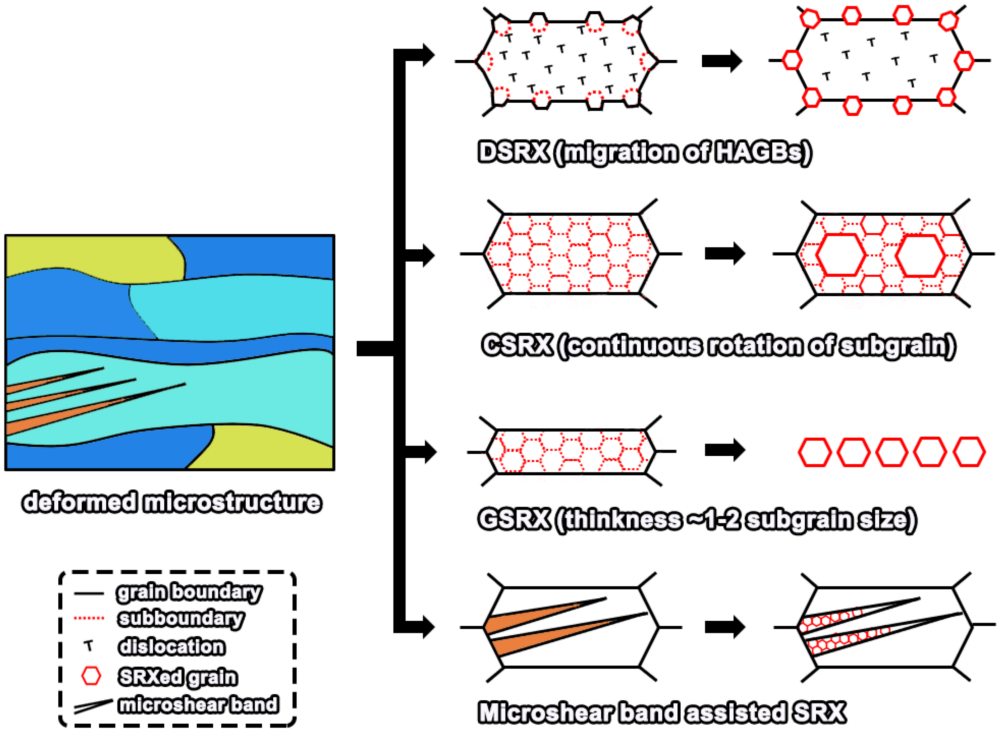


**Figure 7.** Schematic diagram of SRX mechanism of the cold rolling β Ti alloy.

### *3.4. Texture Evolution*

Figure 8 shows the orientation distribution function (ODF) maps of the alloy. As shown in Figure 8a, the ODF map of the cold rolling microstructure exhibits an intensive {111} <112> γ-fiber texture at the Euler angles (30°, 60°, 45°), with a maximum texture intensity of 98.1 mud(multiples of uniform density). Obviously, randomly oriented β grains are slipped and rotated to be consistent, so as to form a strong texture during the rolling process. As the larger grain size of the as-rolled microstructure, the selected area for the EBSD analyses contains insufficient grains and cannot supply accurate information. Then, though the strong rolling texture is obtained, the texture density of 98.1 mud is not reliable. After annealing at 815 °C/2 min (Figure 8b), first the orientation density of {111} <112> γ-fiber texture decreases to 18.3 mud. Second, the {111} <110> texture occurs. It could be attributed to the occurrence of recrystallization which forms randomly oriented recrystallized grains to the decrease of texture intensity. With the extension of holding time, as shown in Figure 8c, the texture intensity peak value decreases continuously to 13.53 mud. Although the change of texture intensity is smaller compared with Figure 8b, the texture is weak α-fiber, γ-fiber, and Goss-fiber, which is {001} <110>, {111} <112>, {111} <123>, {001} <010>, and {112} <110>, respectively. Among the texture components, the {001} <110> texture is the recovered texture, and the Goss-fiber is the recrystallization texture [34]. This phenomenon displays that, with the increase in the holding time, the recovery, and recrystallization degree increase, with the rolling microstructure residual.

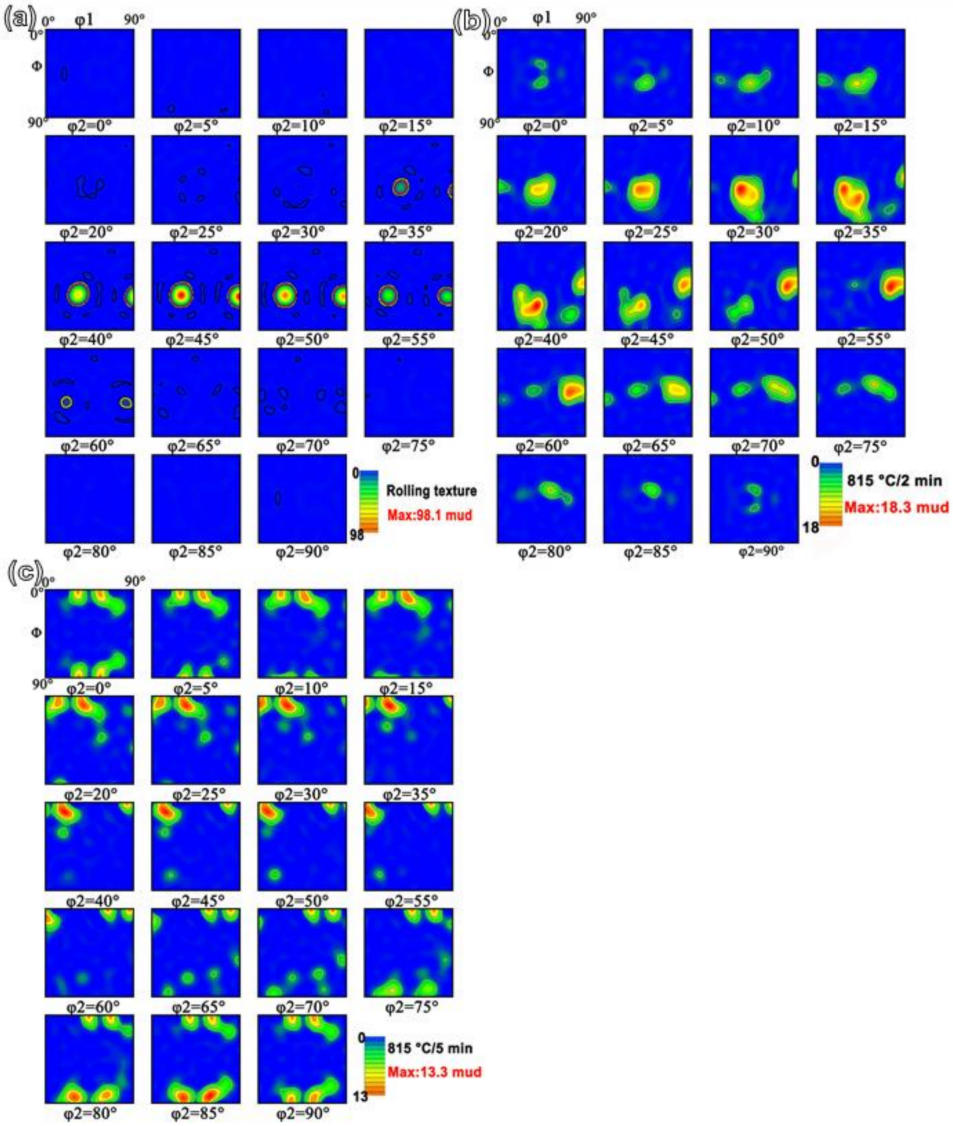


**Figure 8.** Orientation distribution function maps after (**a**) cold rolling; (**b**) cold rolling +815 °C/2 min; and (**c**) cold rolling +815 °C/5 min.

## 4. Conclusions

In the present study, the cold rolling microstructure, static recrystallization mechanism and texture evolution of the beta type Ti alloy were investigated. The main conclusions are summarized as follows:

1. The cold-rolled microstructure is mainly composed of elongated deformed β grains and micro-shear bands. Plenty of fine SRXed grains are obtained after annealing treatment, in the micro-shear band, the grain boundary, and the interior of the deformed grain;
2. Through the annealing treatment, continuous SRX and geometric SRX are observed in the larger deformed microstructure. Besides, the discontinued SRX behavior mainly occurs by the grain boundaries bulging with HAGBs of deformed grains, especially at the trigeminal grain boundaries. Many ultra-fine grains appear inside the micro-shear band, exhibiting a phenomenon of micro-shear band-assisted SRX;
3. The cold rolling microstructure exhibits the typical γ-fiber texture. With the extension of the annealing holding time, the texture type evolves gradually from γ-fiber texture component to weak α-fiber, γ-fiber, and Goss-fiber.

**Author Contributions:** Conceptualization, S.Z., J.H.; methodology, J.H., J.W.; validation, C.Z., X.C.; formal analysis, C.Z.; investigation, X.C., W.Z.; resources, J.H.; data curation, W.Z.; writing—original draft preparation, Q.W.; writing—review and editing, X.C.; funding acquisition, S.Z., J.W. All authors have read and agreed to the published version of the manuscript.

**Funding:** The authors are grateful for financial support from the National Natural Science Foundation of China (52071228, 51901151, 51904205), Key Research and Development program of Shanxi Province (No. 201903D121056 and 201903D421084).

**Institutional Review Board Statement:** Not applicable.

**Informed Consent Statement:** Not applicable.

**Data Availability Statement:** Not applicable.

**Conflicts of Interest:** The authors declare no conflict of interest.

## References

1. Gupta, A.; Khatirkar, R.K.; Kumar, A.; Thool, K.; Suwas, S. Microstructure and texture development in Ti-15V-3Cr-3Sn-3Al alloy-Possible role of strain path. *Mater. Charact.* **2019**, *156*, 109884. [CrossRef]
2. Banerjeea, D.; Williams, J.C. Perspectives on titanium science and technology. *Acta Mater.* **2013**, *61*, 844–879. [CrossRef]
3. Santhosh, R.; Geetha, M.; Rao, M.N. Recent developments in heat treatment of beta titanium alloys for aerospace applications. *Trans. Indian Inst. Met.* **2017**, *70*, 1681–1688. [CrossRef]
4. Boyer, R.R.; Briggs, R.D. The use of β titanium alloys in the aerospace industry. *J. Mater. Eng. Perform.* **2005**, *14*, 681–685. [CrossRef]
5. Cotton, J.D.; Briggs, R.D.; Boyer, R.R. State of the art in beta titanium alloys for airframe applications. *JOM* **2015**, *67*, 1281–1303. [CrossRef]
6. Prasad, S.; Ehrensberger, M.; Gibson, M.P.; Kim, H.; Monaco, E.A. Biomaterial properties of titanium in dentistry. *J. Oral Biosci.* **2015**, *57*, 192–199. [CrossRef]
7. Ivasishin, O.M.; Markovsky, P.E.; Matviychuk, Y.V.; Semiatin, S.L.; Ward, C.H.; Fox, S. A comparative study of the mechanical properties of high-strength β-titanium alloys. *J. Alloy. Compd.* **2008**, *457*, 296–309. [CrossRef]
8. Markovsky, P.E.; Bondarchuk, V.I.; Herasymchuk, O.M. Influence of grain size, aging conditions and tension rate on the mechanical behavior of titanium low-cost metastable beta-alloy in thermally hardened condition. *Mater. Sci. Eng. A* **2015**, *645*, 1502652. [CrossRef]
9. Suwas, S.; Gurao, N.P.; Ali, A. Evolution of transformation texture in a metastable B-titanium alloy. *Mater. Sci. Eng. A* **2009**, *922*, 617–628.
10. Du, Z.X.; Xiao, S.L.; Xu, L.J.; Tian, J.; Kong, F.T.; Chen, Y.Y. Effect of heat treatment on microstructure and mechanical properties of a new β high strength titanium alloy. *Mater. Des.* **2014**, *55*, 183–190. [CrossRef]
11. Xu, T.W.; Li, J.S.; Zhang, S.S.; Zhang, F.S.; Liu, X.H. Cold deformation behavior of the Ti-15Mo-3Al-2.7Nb-0.2Si alloy and its effect on α precipitation and tensile properties in aging treatment. *J. Alloy. Compd.* **2016**, *682*, 404–411. [CrossRef]
12. Qi, L.; Qiao, X.; Huang, L.; Huang, X.; Zhao, X. Effect of cold rolling deformation on the microstructure and properties of Ti-10V-2Fe-3Al alloy. *Mater. Charact.* **2019**, *155*, 109789. [CrossRef]
13. Du, Z.; He, Q.; Chen, R.; Liu, F.; Zhang, J.; Yang, F.; Zhao, X.; Cui, X.; Cheng, J. Rolling reduction-dependent deformation mechanisms and tensile properties in a β titanium alloy. *J. Mater. Sci. Technol.* **2022**, *104*, 183–193. [CrossRef]
14. Lu, S.; Ma, F.; Ping, L.; Li, W.; Liu, X.; Chen, X.; Ke, Z.; Han, Q.; Zhang, L.C. Recrystallization behavior and super-elasticity of a metastable β-type Ti-21Nb-7Mo-4Sn alloy during cold rolling and annealing. *J. Mater. Eng. Perform.* **2018**, *27*, 4100–4106. [CrossRef]
15. Imandoust, A.; Barrett, C.D.; Al-Samman, T.; Tschopp, M.A.; Essadiqi, E.; Hort, N.; El Kadiri, H. Unraveling recrystallization mechanisms governing texture development from rare-earth element additions to magnesium. *Metall. Mater. Trans. A* **2018**, *49*, 1809–1829. [CrossRef]
16. Gupta, A.; Khatirkar, R.K.; Dandekar, T.; Jha, J.S.; Mishra, S. Recrystallization behavior of a cold rolled Ti-15V-3Sn-3Cr-3Al alloy. *J. Mater. Res.* **2019**, *456*, 1–11. [CrossRef]
17. Huang, K.; Log, R.E. A review of dynamic recrystallization phenomena in metallic materials. *Mater. Des.* **2016**, *111*, 548–574. [CrossRef]
18. Imandoust, A.; Barrett, C.D.; Oppedal, A.L.; Whittington, W.R.; Paudel, Y.; El Kadiri, H. Nucleation and preferential growth mechanism of recrystallization texture in high purity binary magnesium-rare earth alloys. *Acta Mater.* **2017**, *138*, 27–41. [CrossRef]
19. Humphreys, F.J.; Hatherly, M. *Recrystallization and Related Annealing Phenomena*, 2nd ed.; Elsevier: Oxford, UK, 2004.
20. Kassner, M.E.; Barrabes, S.R. New developments in geometric dynamic recrystallization. *Mater. Sci. Eng. A* **2005**, *410–411*, 152–155. [CrossRef]
21. Basu, I.; Al-Samman, T.; Gottstein, G. Shear band-related recrystallization and grain growth in two rolled magnesium-rare earth alloys. *Mater. Sci. Eng. A* **2013**, *579*, 50–56. [CrossRef]

22. Zhou, J.H.; Shen, Y.F.; Xue, W.Y.; Jia, N. Hot-deformation induced static recrystallization and nano-MX precipitation in a low activation martensitic steel. *J. Nucl. Mater.* **2021**, *556*, 153190. [CrossRef]
23. Zhao, L.Y.; Yan, H.; Chen, R.S.; Han, E.H. Orientations of nuclei during static recrystallization in a cold-rolled Mg-Zn-Gd alloy. *J. Mater. Sci. Technol.* **2021**, *60*, 162–167. [CrossRef]
24. Zhao, L.Y.; Yan, H.; Chen, R.S.; Han, E.-H. Study on the evolution pattern of grain orientation and misorientation during the static recrystallization of cold-rolled Mg-Zn-Gd alloy. *Mater. Charact.* **2019**, *150*, 252–266. [CrossRef]
25. Zeng, Z.R.; Zhu, Y.M.; Xu, S.W.; Bian, M.Z.; Davies, C.H.J.; Birbilis, N.; Nie, J.F. Texture evolution during static recrystallization of cold-rolled magnesium alloys. *Acta Mater.* **2016**, *105*, 479–494. [CrossRef]
26. Zhao, L.Y.; Yan, H.; Chen, R.S.; Han, E.H. Oriented nucleation causing unusual texture transition during static recrystallization annealing in cold-rolled Mg-Zn-Gd alloys. *Scr. Mater.* **2020**, *188*, 200–205. [CrossRef]
27. Mittemeijer, E.J. *Fundamentals of Materials Science*, 1st ed.; Springer: Berlin, Germany, 2010.
28. Radhakrishnan, B.; Sarma, G.B.; Zacharia, T. Modeling the kinetics and microstructural evolution during static recrystallization-Monte Carlo simulation of recrystallization. *Acta Mater.* **1998**, *46*, 4415–4433. [CrossRef]
29. Henshall, G.A.; Kassner, M.E.; Mcqueen, H.J. Dynamic restoration mechanisms in Al-5.8 At. Pct Mg deformed to large strains in the solute drag regime. *Metall. Trans. A* **1992**, *23*, 881–889. [CrossRef]
30. McQueen, H.J.; Knustad, O.; Ryum, N.; Solberg, J.K. Microstructural evolution in Al deformed to strains of 60 at 400 °C. *Scr. Metall. Mater.* **1985**, *19*, 73–78. [CrossRef]
31. Gholinia, A.; Humphreys, F.J.; Prangnell, P.B. Production of ultra-fine grain microstructures in Al-Mg alloys by coventional rolling. *Acta Mater.* **2002**, *50*, 4461–4476. [CrossRef]
32. Solberg, J.K.; McQueen, H.J.; Ryum, N.; Nes, E. Influence of ultra-high strains at elevated temperatures on the microstructure of aluminium. *Part I Philos. Mag. A* **1989**, *60*, 447–471. [CrossRef]
33. Wu, W.X.; Jin, L.; Zhang, Z.Y.; Ding, W.J.; Dong, J. Grain growth and texture evolution during annealing in an indirect-extruded Mg-lGd alloy. *J. Alloy. Compd.* **2014**, *585*, 111–119. [CrossRef]
34. Raabe, D.; Luecke, K. Rolling and annealing textures of bcc metals. *Mater. Sci. Forum.* **1994**, *157*, 597–610. [CrossRef]